Fig. 7.2.5: Plots of slope against position along the circular sections of the assumed toroidal wavefront in the G60 tilt: (a) $u^{60}(x_R{}^{60})$; (b) $v^{60}(y_R{}^{60})$.

be reliable ones. However, in the G90 tilt and the G60 tilt cases acceptable fits were attained along the directions of the principal meridians of the surface, and two different radii of curvature were measured for the toroidal wavefront incident on the Ronchi ruling. The values obtained in both orientations of sample P30025A may be seen to be quite similar. The angular misalignment values, that is, the angular values associated with tilts and displacements of the sample surface relative to the incident wavefront, have quite different values in both orientations of the sample, as could be expected from Fig. 7.2.4a and 7.2.4b, where both data sets can be seen to impinge on different areas of the Ronchi ruling, because of the different misalignments of the sample relative to the incident wavefront at both orientations. It must be observed that an additional misalignment possibility has been introduced in the experimental setup through the rotation of the samples, unless the vertex of the sample surface is placed exactly at the Z axis of the experimental setup.

We have thus been able to measure a toroidal wavefront using our approach to Ronchi deflectometry. The next step is to ray-trace these slopes and positions at the Ronchi ruling to the tangent plane to the sample surface at its vertex, and, using the known position of the source, to measure the local normals to the sample surface at a set of points. No data on the reflected wavefront at the tangent plane to the surface is provided, as in Section 6.2 it was shown to be almost equivalent to the values of

curvature and misalignment obtained at the surface. It should be remembered that the similarity of the values of the reflected wavefront to those of the surface were used in Section 6.2 to justify ray-tracing to the tangent plane to the surface instead of to the surface itself under our experimental outline.

Figure 7.2.6 shows the different plots representing position against position, and the components of the local normal against their corresponding position values for the G60 and G90 tilts. Conclusions are similar to those of Fig. 7.2.4: two different slope values may be seen in Fig. 7.2.6c and 7.2.6e, following a linear plot as in the case of G90 these sections of the toroidal surface coincide with the principal meridians of the surface. When comparing Fig.7.2.6 with Fig.7.2.4, however, the slope difference is smaller between both meridians. In the case of G60 the $N_X(x_S)$ and $N_Y(y_S)$ plots are not so close to straight lines as they do not follow any circular section of the toroidal surface. However, the departure from the theoretical straight line is less noticeable than in Fig. 7.2.4d or 7.2.4f. When the same graphs are plotted following the direction of the circular sections of the toroidal surface, plots closer to the linear shape are obtained (Fig. 7.2.7). These plots of the components of the local normal along the principal meridian direction will hereafter be named $N_X^{60}(x_R^{60})$ and $N_Y^{60}(y_R^{60})$.

Table 6.2.2 shows the fitted values for the curvature and angular misalignment of the surface. The radius of curvature values thus obtained are the ones that will be used as final results of our measurement using two-dimensional fitting.

Table 7.2.2: Two-dimensional fitting results for the curves corresponding to the G90 and G60 tilts, and to the circular sections of the G60 tilt measurement on the tangent plane to the surface. A $y=C\xi+K$ curve was fitted with ξ being either x_R, y_R, x_R^{60} or y_R^{60}. y may be either N_X, N_Y, N_X^{60} or N_Y^{60}. C stands for curvature, K for angular misalignment, r^2 for the correlation coefficient and R for the measured radius of curvature of the sample.

Sample P30025A		**C(mm^{-1})**	**K(rad)**	**r^2**	**R(mm)**
G90	**N_X (x_R)**	$5.8093\ 10^{-3}$	$-2.2969\ 10^{-3}$	0.999998	172.14
	N_Y (y_R)	$6.2176\ 10^{-3}$	$7.1790\ 10^{-3}$	0.999998	160.83
G60	**N_X (x_R)**	$5.8943\ 10^{-3}$	$-2.6519\ 10^{-3}$	0.999075	169.65
	N_Y (y_R)	$6.0941\ 10^{-3}$	$9.7510\ 10^{-4}$	0.999070	164.09
G60 rotated	**$N_X^{60}(x_R^{60})$**	$5.8045\ 10^{-3}$	$2.6617\ 10^{-3}$	0.999998	172.28
	$N_Y^{60}(y_R^{60})$	$6.2219\ 10^{-3}$	$-5.9517\ 10^{-4}$	0.999994	160.72

Fig. 7.2.6: Measured sample surface; (a) $y_R(x_R)$ for the G90 tilt; (b) $y_R(x_R)$ for the G60 tilt; (c) $N_X(x_R)$ for the G90 tilt; (d) $N_X(x_R)$ for the G60 tilt; (e) $N_Y(y_R)$ for the G90 tilt; (f) $N_Y(y_R)$ for the G60 tilt.

Fig. 7.2.7: Plots of components of the local normal against position along the circular sections of the assumed toroidal wavefront in the G60 tilt: (a) $N_X^{60}(x_R^{60})$ plot ; (b) $N_Y^{60}(y_R^{60})$ plot.

As expected from the plots, a reduction in curvature differences when comparing both principal meridians is observed, and the plots not aligned with the principal meridians display better correlation coefficients than the equivalent values in the Ronchi ruling plane. However, the linear fits achieved along the circular sections of the surface are much better than the ones obtained along directions different from those of the principal meridians (shadowed rows in Table 7.2.2). The robustness of the technique will be further studied in Section 7.3, but the curvature values obtained for the G60 and G90 tilts along the principal meridians of the surface are quite close to each other. It is interesting to notice how the radius of curvature values not fitted along the principal meridians have intermediate curvature values from those obtained at the principal meridians. Angular misalignment values still vary with the rotation of the sample, as it depends on the position of the vertex of the surface and its rotation axis relative to the Z axis of our experimental setup. Although comparison of the final radius of curvature values with the reference estimate will be performed in Section 7.2.3, these values may be seen to be quite close to the values provided for sample P30025A in Table 7.1.2. So, radius of curvature measurements of toroidal surfaces have been performed regardless of the sample's orientation [Arasa 1998][Royo 1998].

Once the local normals to the surface and their relative positions have been determined, the surface reconstruction step may be performed and three-dimensional fitting procedures obtained. The sampled area and height range values of the topographic reconstruction are close to the ones obtained with spherical samples. The measured area is 257.1mm^2 and the measured height range is 0.42mm in the G90 tilt measurement, while in the G60 tilt the measured area is 278.9mm^2 and the measured height range is 0.45mm [Royo 1999]. In Section 7.3 these will be shown to be typical values of our approach to the Ronchi test technique.

Fig. 7.2.8 shows the three-dimensional plot and residual for both G90 and G60 tilts of the sample. In this case, residuals are the differences of the sampled data points relative to the best fitted spherocylindrical surface (see Section 7.1). Notice how the sharp edges in the residual plot correspond to software interpolation of the surface of the residuals; data points present smooth variations in the available field of view.

As previously seen in Section 6.2, this sort of three-dimensional plot is very spectacular but it becomes difficult to compare them in subjects such as, for instance, the rotation of the sample. Pseudocolor contour plots with fixed step increments along each of the samples provide an easier comparison of the results. Again, our decision was to fix step increments in all the measurements of a given sample. This means that, as our integration procedures do not leave all surfaces with their vertex at a given height, some small absolute positioning differences between topographies might be seen. However, the shape of the reconstructed surface is suitably obtained at each measurement, as may be seen either in the topographic pseudocolor plots or in the three-dimensional fitting results.

Fig. 7.2.9 again presents the data of Fig. 7.2.8 in the form of pseudocolor plots, so the reader may compare both kinds of representations. In Fig.7.2.9 the contour step of the topography plots was set at 29μm and the contour steps of the residual plots at 49nm. This kind of plot allows us to see qualitatively how topographies of tilted samples are tilted by the same amount. It is again stated that the blue contour line stands for minimum deviations from the best fit spherocylindrical surface. Notice how residual plots of the G60 and G90 tilts have three almost parallel blue bands, which may be seen in Fig. 7.2.9b and 7.2.9d. These three blue bands may be seen to rotate at both residual plots following the rotation of the sample surface. As in the case of spherical surfaces, pseudocolor contour plots will be adopted for all remaining topographic and residual plots because of their ease of interpretation.

Fig. 7.2.8: Three-dimensional plots: (a) Topography, G90 tilt; (b) Residual from the best fit ,G90 tilt; (c) Topography,G60 tilt ; (d) Residual from the best fit,G60 tilt

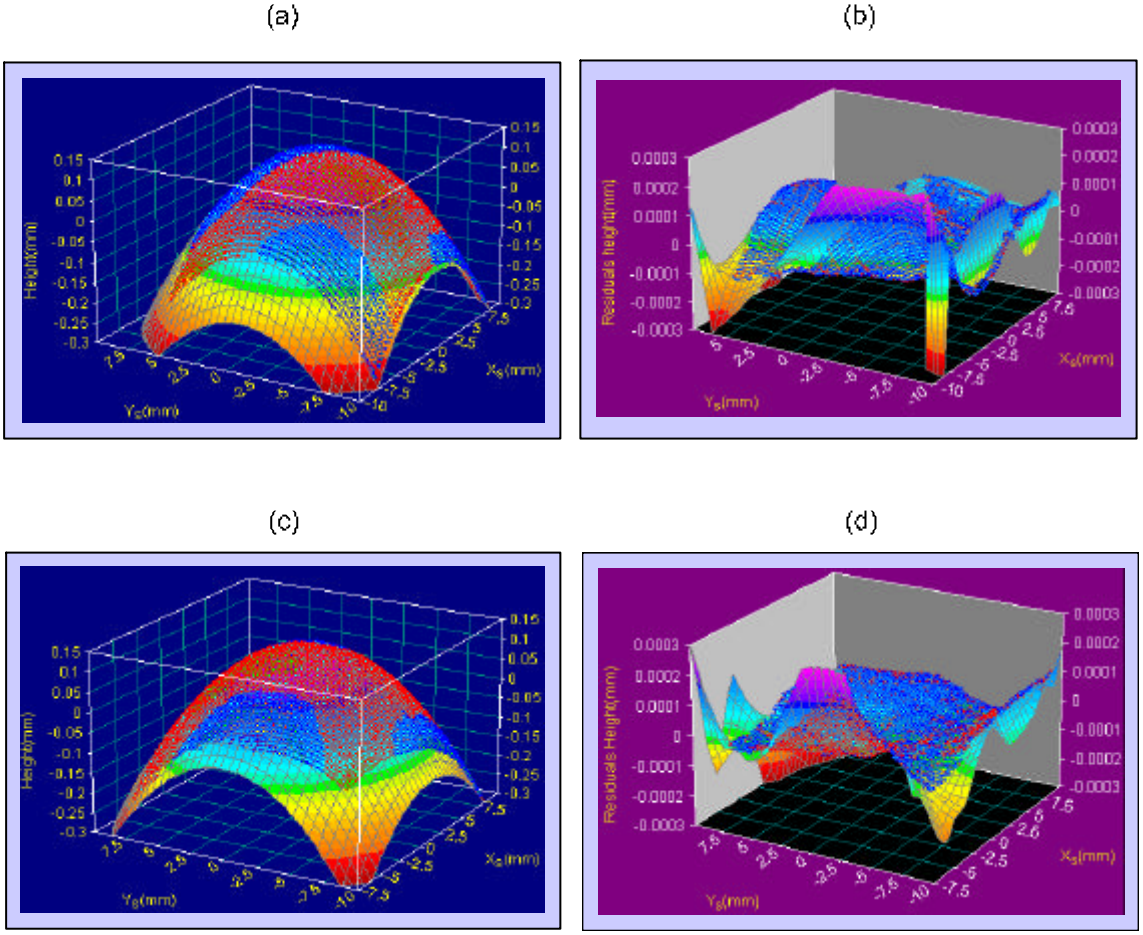

Table 7.2.3 shows the values obtained when performing three-dimensional fitting procedures to the measured data. A spherocylindrical surface described as

$$\begin{aligned} x - x_0 &= x_S \cos\theta + y_S \operatorname{sen}\theta \\ y - y_0 &= -x_S \operatorname{sen}\theta + y_S \cos\theta \end{aligned} \qquad (7.2.1)$$

$$z = \frac{\dfrac{(x-x_0)^2}{R_1} + \dfrac{(y-y_0)^2}{R_2}}{1 + \sqrt{1 - \dfrac{\left[\dfrac{(x-x_0)^2}{R_1} + \dfrac{(y-y_0)^2}{R_2}\right]^2}{(x-x_0)^2 + (y-y_0)^2}}}$$

Fig. 7.2.9: Pseudocolor plots. (a) Topography, G90 tilt; (b) Residual from the best fit, G90 tilt; (c) Topography, G60 tilt; (d) Residual from the best fit,G60 tilt. The contour step is 29μm in the topography plots and 49nm in the residual plots.

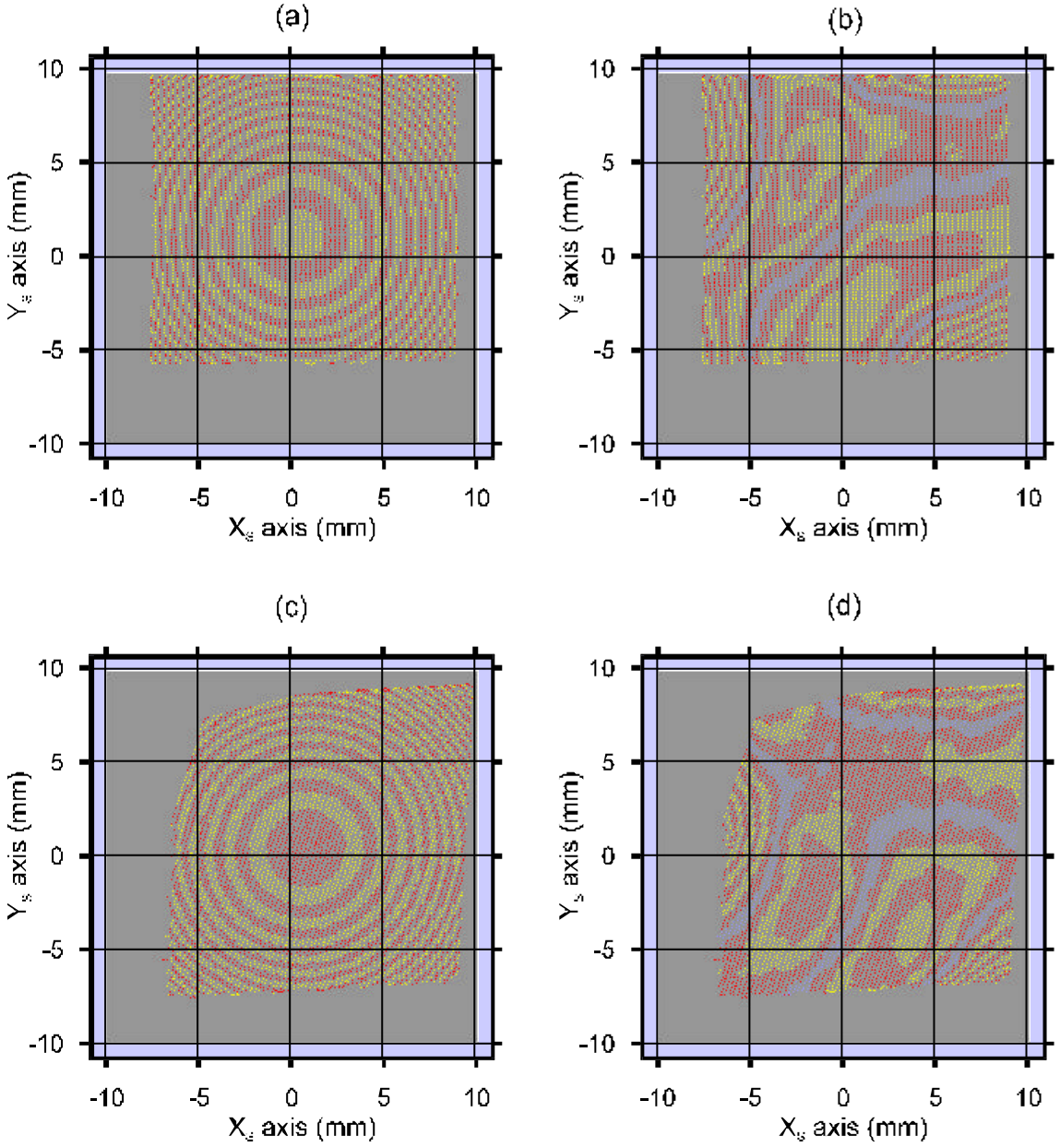

where the parameters to fit will be R_1, R_2, radius of curvature of the toroidal surface along its principal meridians; (x_0,y_0), position of the vertex of the surface, and θ direction of the principal meridians. x and y are simply tilted coordinates from the measured x_S and y_S values. This should not be considered as being a parametric equation, as all coordinates are combined in a single expression valid in the complete spatial domain. Eq.7.2.1 has been divided into three parts in order to make it more

understandable to the reader. It should be noted that R_1 and R_2 may be either the radius of curvature of the base curve of the surface or the cross curve of the surface, (R_B or R_C), as both curves may be placed along the X or Y axis. Furthermore, the θ parameter may display two valid angular values, that is α and α+90°, depending on the position of the considered meridian. In our Tables, θ will always be given a value between 0 and 90°. So θ should be considered the angular position of the principal meridian placed in the 0°-90° interval, that is, in the first quadrant.

Table 7.2.3: Results of fitting the measured data to a spherocylindrical surface (Eq. q. 7.2.1). R_B stands for the radius of curvature of the base curve of the toroidal surface; R_C for the radius of curvature of the cross curve; (x_0,y_0) for the measured coordinates of the vertex of the surface; θ for the direction of the principal meridian contained in the first quadrant; r^2 for the correlation coefficient of the fit.

Sample P30025A	R_B(mm)	R_C(mm)	x_0(mm)	y_0(mm)	q(°)	r^2
G90	171.87	160.96	0.3945	1.1545	0.1	0.9999993
G60	172.42	160.47	0.0388	0.8947	59.3	0.9999996

The curve-fitted results agree quite well in the measured radius of curvature values of the base and cross curves of the toroidal surface, which are very close to each other. The direction of the principal meridians is also suitably calculated by the θ parameter, which greatly coincides with the theoretical tilt applied to the sample. The vertex of the surface position, although varying from one tilt to another, is also easily measured through curve fitting.

To sum up, a full topographic reconstruction and radius of curvature measurement process has been carried out at two tilted orientations of a toroidal sample, showing the main differences of its measuring process relative to what was presented in Section 6.2 for spherical surfaces. Radius of curvature measurements have been made using both two-dimensional and three-dimensional procedures. Two dimensional procedures will work, given that the slope against position curve considered was taken along a circular section of the toroidal surface. In Section 7.3 complete results for the six samples described in Table 7.1.2 will be presented.

7.2.2.- Error analysis

In order to continue with the pattern used in Section 6.2, the numerical results for the data in the G60 and G90 tilts will be presented, in the form of the standard deviations and confidence intervals of two and three-dimensional curve-fitting procedures. The estimate for the accuracy in the measurement of a single slope value is still $C_x = 8.61\ 10^{-3} \pm 1.8\ 10^{-4}$ mm^{-1}, as calculated in Section 4.3.1. As the uncertainty in the quality of the fitting procedure depends on the experimental values available, these will be presented in detail for the G90 and G60 tilts, as part of the typical experiment presented in this Section.

The closeness of all correlation coefficients to unity allows a prediction that all standard deviation values will be very small, and confidence intervals very narrow. This may be seen in Table 7.2.4, where the absolute and relative values for standard deviation and the interval where the "real" measured value may be found with 0.95 probability are described for the two-dimensional fitting procedures of the G60 and G90 tilts. Only fittings along the principal meridians of the toroidal surface will be considered.

Table 7.2.4: Error analysis in two-dimensional curve-fitted curvature values for the X and Y directions of the G60 and G90 tilts. σ stands for the standard deviation of the data, $\%\sigma$ for its relative value, C_{MIN}^{95} and C_{MAX}^{95} for the limits of the confidence interval where the real curvature value is found within a probability of 0.95, R for the radius of curvature and ΔR for its variation in the interval of curvatures $C \pm \sigma$.

Sample P30025A		C (mm^{-1})	s (mm^{-1})	%s	C_{MIN}^{95} (mm^{-1})	C_{MAX}^{95} (mm^{-1})	R (mm)	DR (mm)
G90	$N_X(x_S)$	$5.8093\ 10^{-3}$	$1.1\ 10^{-7}$	$2\ 10^{-3}$	$5.8091\ 10^{-3}$	$5.8095\ 10^{-3}$	172.14	$6.5\ 10^{-3}$
	$N_Y(y_S)$	$6.2176\ 10^{-3}$	$1.2\ 10^{-7}$	$2\ 10^{-3}$	$6.2174\ 10^{-3}$	$6.2178\ 10^{-3}$	160.83	$6.2\ 10^{-3}$
G60	$N_X^{60}(x_S^{60})$	$5.8045\ 10^{-3}$	$8.4\ 10^{-8}$	$1\ 10^{-3}$	$5.8043\ 10^{-3}$	$5.8046\ 10^{-3}$	172.28	$5.0\ 10^{-3}$
	$N_Y^{60}(y_S^{60})$	$6.2219\ 10^{-3}$	$1.8\ 10^{-7}$	$3\ 10^{-3}$	$6.2215\ 10^{-3}$	$6.2222\ 10^{-3}$	160.72	$9.3\ 10^{-3}$

Standard deviations in all fits have extremely low values, as they are all microstepped experiments with a large amount of data points and good correlation coefficients. These standard deviations are comparable to the ones obtained in Section 6.2.2 for spherical surfaces, in the microstepped experiments. The intervals of confidence and the radius of curvature variations in the $C \pm \sigma$ interval show that limits in

the measurement technique will not be placed by the uncertainties in the fitting procedures, but by the uncertainties embedded in the experimental setup, which were described in Section 4.3.1 and are much larger than the ones introduced in the curve-fitting procedures.

An error analysis on angular misalignment values will also be performed this way, as was done in the case of spherical surfaces. Their results may be seen in Table 7.2.5, and give the same conclusions as those of Table 7.2.4: fitting uncertainties are one hundred times smaller than slope measurement uncertainties, and these values are fully comparable to the ones we obtained when developing spherical surface topographies (see Table 6.2.6).

Table 7.2.5: Error analysis in two-dimensional curve-fitted angular misalignment values for the X and Y directions of the G60 and G90 tilts. K stands for angular misalignment, σ for the standard deviation of the data, $\%\sigma$ for its relative value, K_{MIN}^{95} and K_{MAX}^{95} for the limits of the confidence interval where the real curvature value is found within a probability of 0.95,

Sample P30025A		K(rad)	σ (rad)	$\%\sigma$	K_{MIN}^{95} (rad)	K_{MAX}^{95} (rad)
G90	$N_X(x_S)$	$-2.2969\ 10^{-3}$	$5.5\ 10^{-7}$	0.02	$-2.2981\ 10^{-3}$	$-2.2959\ 10^{-3}$
	$N_Y(y_S)$	$7.1790\ 10^{-3}$	$5.8\ 10^{-7}$	$8\ 10^{-3}$	$7.1778\ 10^{-3}$	$7.1801\ 10^{-3}$
G60	$N_X^{60}(x_S^{60})$	$2.6617\ 10^{-3}$	$4.2\ 10^{-7}$	0.02	$2.6608\ 10^{-3}$	$2.6625\ 10^{-3}$
	$N_Y^{60}(y_S^{60})$	$-5.9517\ 10^{-4}$	$8.2\ 10^{-7}$	0.14	$-5.9677\ 10^{-3}$	$-5.9356\ 10^{-3}$

Three dimensional curve-fitting procedures will also be analyzed this way, although we must expect results similar to the ones presented as the correlation coefficients are also close to unity and the amount of data points involved is quite large. The main difference will be that no circular section of the surface needs to be assumed, as the fitting will involve the whole surface, and that a spherocylindrical surface shape is being assumed as an approximation to the real toroidal surface of the samples. Table 7.2.6 presents the absolute and relative standard deviation, and the confidence intervals for 0.95 probability, for the five parameters involved in three-dimensional curve-fitting, that is R_B, R_C, x_0, y_0 and θ. Results are presented for the G90 and G60 tilts.

Table 7.2.6 closely follows the conclusions drawn from the error analysis of Tables 7.2.4 and 7.2.5. The limits to the measurement technique are placed in the experimental setup, as the standard deviations of the fitted data are very small, and

lead to confidence intervals in radius of curvature measurements around 0.01mm, both in two-dimensional and three-dimensional curve fitting procedures. Such accuracy is beyond our experimental limits, as, for instance, the differences in the measured radius of curvature of the surface are around 0.5mm when comparing the values obtained using the G60 and G90 tilts. Enhancements to the measurement technique will involve improvements in the quality and stability of the measurements through enhancements in the experimental setup.

Table 7.2.6: Error analysis in three-dimensional curve fitting, for the radius of curvature of the base curve (R_B) and the cross curve (R_C), the vertex position of the sample surface (x_0 and y_0), and the direction of the principal meridian present in the first quadrant (θ). σ stands for standard deviation, $\%\sigma$ for its relative value and ξ for the variable considered in the corresponding row.

Sample P30025A		Fit	σ	$\%\sigma$	$\xi_{95\,MIN}$	$\xi_{95\,MAX}$
G90	R_B(mm)	171.87	$2.6\ 10^{-3}$	$2\ 10^{-3}$	171.86	171.87
	R_C(mm)	160.96	$2.5\ 10^{-3}$	$2\ 10^{-3}$	160.95	160.96
	x_0(mm)	0.3945	$1.1\ 10^{-4}$	0.03	0.3943	0.3948
	y_0(mm)	1.1545	$5.4\ 10^{-5}$	$5\ 10^{-3}$	1.1544	1.1546
	θ(°)	0.11	$5.8\ 10^{-3}$	$6\ 10^{-3}$	0.11	0.13
G60	R_B(mm)	172.42	$1.7\ 10^{-3}$	$1\ 10^{-3}$	172.42	172.43
	R_C(mm)	160.47	$1.9\ 10^{-3}$	$1\ 10^{-3}$	160.47	160.48
	x_0(mm)	0.0388	$1.1\ 10^{-4}$	0.28	0.0386	0.0390
	y_0(mm)	0.8948	$2.5\ 10^{-5}$	$2\ 10^{-3}$	0.8947	0.8948
	θ(°)	59.32	$6.4\ 10^{-3}$	0.01	59.31	59.33

7.2.3.- Validity of the measured values

Once the measurement of radius of curvature and its accuracy have been calculated, we have to consider how far the obtained values coincide with the reference ones. All measured radii values are presented in Table 7.2.7. However, it should be remembered that the reference radius of curvature values provided by the Möller-Wedel high precision radioscope lack the accuracy of the measurements achieved in spherical surfaces. The radioscope only provides a rough estimate of the measurements with an uncertainty around $\pm$1mm.

Table 7.2.7: Comparison of measured radius of curvature with the reference Möller-Wedel radioscope measurement. % deviation refers to relative differences between the measured and radioscope values for the base and cross curves.

Measurement method		R_B(mm)	s (mm)	R_C(mm)	s (mm)	%Deviation	
2D fitting	G90	172.1	$3.4\ 10^{-3}$	160.8	$3.0\ 10^{-3}$	0.1	0.7
	G60	172.3	$2.5\ 10^{-3}$	160.7	$4.7\ 10^{-3}$	0.2	0.6
3D fitting	G90	171.9	$2.6\ 10^{-3}$	161.0	$2.5\ 10^{-3}$	0.1	0.2
	G60	172.4	$1.7\ 10^{-3}$	160.7	$1.9\ 10^{-3}$	0.2	0.6
Möller-Wedel radioscope		172.0±1.0mm		159.7±1.0mm			

With this consideration in mind, the deviations of the measured radius of curvature of the base and the cross curves using Ronchi deflectometry and direct measurement through the radioscope should only be considered as a comparison between radius of curvature values measured using different techniques, as no reliable reference is available. However, the dispersion of the radius of curvature values measured with two-dimensional fitting, three-dimensional fitting and radioscope measurements is very small, showing the technique to be reliable. All measurements performed using our approach to Ronchi deflectometry show a maximum dispersion of 0.8mm in their values, which is inside the uncertainty range of 2% which was fixed in Section 4.3.1. This uncertainty value has to be considered as an overestimate, as, according to the measured results, the technique may be assumed to measure radius of curvature of toroidal surfaces with an accuracy of at least ±1mm, which amounts to just a 0.6% relative error.

As in the case of spherical surface measurements, no validation procedure was available for our surface topographies and residuals. However, in the following section it will be seen how the same topography and residual is repeatedly obtained in all positions and tilts of the sample, and how tilted sample positions give topographies tilted by the same amount, as could be observed from the residuals in Fig. 7.2.9.